



1 **Monitoring of glacier albedo from optical remote-sensing data:**
2 **application to seasonal and annual surface mass balances**
3 **quantification in the French Alps for the 2000-2015 period**

4

5

6 Lucas Davaze¹, Antoine Rabatel¹, Yves Arnaud¹, Pascal Sirguey², Delphine Six¹, Anne
7 Letreguilly¹, Marie Dumont³

8

9

10 ¹ Université Grenoble Alpes, CNRS, IRD, Grenoble INP, IGE, F- 38000 Grenoble, France

11 ² National School of Surveying, University of Otago, Dunedin, New Zealand

12 ³ Météo France, CNRS, CNRM – UMR3589, CEN, F-38000 Grenoble, France

13

14

15

16 *Correspondence to:* L. Davaze (lucas.davaze@univ-grenoble-alpes.fr)

17

18



19 **Abstract.**

20 Less than 0.25% of the 250,000 glaciers inventoried in the Randolph Glacier Inventory (RGI
21 V.5) are currently monitored with in situ measurements of surface mass balance. Increasing
22 this archive is very challenging, especially using time-consuming methods based on in situ
23 measurements, and complementary methods are required to quantify the surface mass balance
24 of unmonitored glaciers. The current study relies on the so-called albedo method, based on the
25 analysis of albedo maps retrieved from optical satellite imagery acquired since 2000 by the
26 MODIS sensor, onboard of TERRA satellite. Recent studies revealed substantial relationships
27 between summer minimum glacier-wide surface albedo and annual surface mass balance,
28 because this minimum surface albedo is directly related to the accumulation-area ratio and the
29 equilibrium-line altitude.

30 On the basis of 30 glaciers located in the French Alps where annual surface mass balance are
31 available, our study conducted on the period 2000-2015 confirms the robustness and reliability
32 of the relationship between the summer minimum surface albedo and the annual surface mass
33 balance. At the seasonal scale, the integrated summer surface albedo is significantly correlated
34 with the summer surface mass balance of the six glaciers seasonally monitored. For the winter
35 season, four of the six glaciers showed a significant correlation when linking the winter
36 surface mass balance and the integrated winter surface albedo, using glacier-dependent
37 thresholds to filter the albedo signal (threshold from 0.53 to 0.76). These results are promising
38 to monitor both annual and seasonal glacier-wide surface mass balances of individual glaciers
39 at a regional scale using optical satellite images. A sensitivity study on the computed cloud
40 masks revealed a high confidence in the retrieved albedo maps, restricting the number of
41 omission errors. Albedo retrieval artifacts have been detected for topographically incised
42 glaciers, highlighting limitations in the shadows correction algorithm, although inter-annual
43 comparisons are not affected by systematic errors.

44



45 **1 Introduction**

46 Mountain glaciers represent only 3% of the ice volume on the Earth but contribute
47 significantly to sea level rise (Church et al., 2013; Ohmura, 2004). In addition, millions of
48 people partly rely on glaciers, either for drinking water, agriculture or related glacier hazards
49 (Chen and Ohmura, 1990; Immerzeel et al., 2010; Kaser et al., 2010). The surface mass
50 balance (SMB) of glaciers is directly driven by the climate conditions; consequently, glaciers
51 are among the most visible proxies of climate change (Stocker et al., 2013). Measuring and
52 reconstructing glacier SMB therefore provides critical insights on climate change both at
53 global and regional scales.

54 Systematic SMB monitoring programs began in the late 1940s - early 1950s in most of the
55 European countries (e.g., Sweden, France, Switzerland, Norway). Gradually, more glaciers
56 have become monitored, reaching the present worldwide figure of 440. However, this
57 represents only a little sample of the nearly 250,000 inventoried glaciers worldwide (Pfeffer et
58 al., 2014). Among the existing methods to quantify changes in glacier SMB, the well-
59 established glaciological method has become a standard widely used worldwide yielding most
60 of the reference datasets (World Glacier Monitoring Service, WGMS, Zemp et al., 2015).
61 Based on repeated in situ measurements, this method requires intensive fieldwork. This
62 method is however unable to reconstruct SMB of unmonitored glaciers. The Global Terrestrial
63 Network for Glaciers (GTN-G) aims at increasing substantially the number of monitored
64 glaciers to study regional climate signal through changes in SMB. To this aim, the
65 development of methods complementary to the ground-based glaciological method is therefore
66 required. Since the 1970s, several methods have taken advantage of satellite imaging to
67 compute changes in glacier volume. Several glacier surface properties have thus been used as
68 proxies for volume fluctuations: changes in surface elevation from differencing digital
69 elevation models (DEM) (e.g., Berthier et al., 2016; Gardelle et al., 2013); end-of-summer
70 snow line elevation from high spatial resolution optical images (e.g. Meier and Post, 1962;
71 Rabatel et al., 2005, 2008, 2016); mean regional altitude of snow from low spatial resolution



72 optical images (Drolon et al., 2016); or changes in the glacier surface albedo from high
73 temporal resolution images (Brun et al., 2015; Dumont et al., 2012; Sirguey et al., 2016).
74 Often used over icecaps or large ice masses, satellite derived DEM are not accurate enough to
75 compute confident annual volume changes of mountain glaciers, even if recent studies have
76 revealed promising results for multi-year glacier surface elevation changes of large
77 mountainous glacierized areas (Kääb et al., 2015). The method based on the correlation
78 between the regional snow cover and glacier SMB have shown satisfying results to retrieve
79 seasonal SMB, especially for the winter period. This method allowed the quantification of 55
80 glaciers SMB in the European Alps over the period 1998-2014 (Drolon et al., 2016). However,
81 this method still relies on calibration with field data and requires improvements for summer
82 and annual SMB. The method based on the identification on high spatial resolution optical
83 images of the end-of-summer snow line altitude has shown encouraging results in the French
84 Alps, multiplying by six the available long-term annual SMB time series (Rabatel et al., 2016),
85 but need to be automatized to compute glacier SMB at regional scales. In addition, monitoring
86 glacier surface properties on the daily or weekly basis and over large glacierized regions is still
87 challenging with high spatial resolution images. The current study is based on the albedo
88 method (Brun et al., 2015; Dumont et al., 2012; Sirguey et al., 2016). Images from the
89 MODerate resolution Imaging Spectroradiometer (MODIS) are processed to compute daily
90 albedo map of 30 glaciers in the French Alps over the period 2000-2015. Then, we rely on the
91 methodological framework proposed by Sirguey et al. (2016) on Brewster Glacier (New-
92 Zealand), looking at the relationships between annual and seasonal SMB and the glacier-wide
93 averaged surface albedo $\bar{\alpha}$. Our overall objective is to study the relationships between glacier
94 SMB and albedo by: (i) reconstructing the annual albedo cycle for 30 glaciers in the French
95 Alps for the period 2000-2015; (ii) linking the albedo signal to the seasonal components of the
96 SMB as well as to its annual values for 6 and 30 glaciers, respectively; (iii) assessing the
97 sensitivity of the retrieved albedo towards tuning parameters (cloud coverage threshold for



98 images processing, threshold on the winter albedo signal). Section 2 presents the available
99 SMB datasets used for the comparison and describes briefly the in situ automatic weather
100 stations (AWS) used to assess the quality of MODIS retrieved albedo. The method to retrieve
101 albedo maps is described in Sect. 3. Results are presented and discussed in Sect. 4 and 5. The
102 conclusion gathers the main results of the study and provides perspectives for future works.

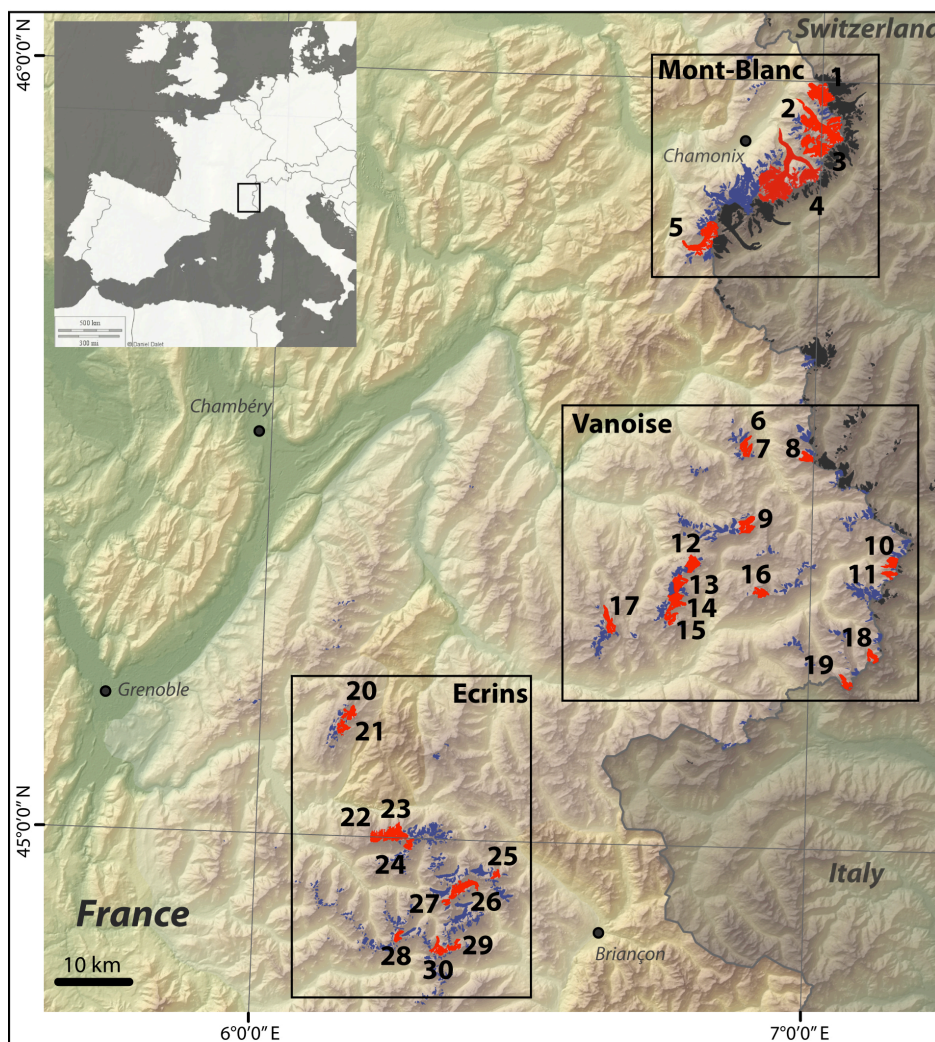
103 **2 Study area and data**

104 **2.1 Site description**

105 The study focuses on 30 glaciers located in the French Alps (Fig. 1). Each glacier can be
106 classified as mountain glacier, extending over an altitudinal range from around 1600 m a.s.l.
107 (Argentière and Mer de Glace glaciers) to 4028 m a.s.l. (Blanc Glacier), and located between
108 the coordinates: 44°51' N to 46° N and 6°09' E to 7°08' E. The cumulative glacial coverage
109 considered in the present study is 136 km², i.e. half of the glacier surface area covered by 593
110 inventoried glaciers over the French Alps for the period 2006-2009 (Gardent et al., 2014).

111 Studied glaciers have been selected following four criteria related to the availability of field
112 data and remote sensing constraints, namely: (i) the annual glacier-wide SMB for the study
113 period had to be available; (ii) the glacier surface area had to be wide enough to allow robust
114 multi-pixel analysis; (iii) the glacier had to be predominantly free of debris to allow remotely-
115 sensed observations of the albedo of snow and ice surfaces; and (iv) seasonal SMB records
116 had to be available to consider seasonal variability. Finally, 11 glaciers have been selected in
117 the Ecrins range, 14 in Vanoise and 5 in Mont-Blanc (Fig. 1, and listed Table 1).

118



119

120 **Figure 1** Map of the region of interest with the studied glaciers shown in red (numbers refer to
121 Table 1). The four AWS used in the present study were set up on Saint-Sorlin Glacier (n°20).
122 Adapted from Rabatel et al. (2016).

123

124 2.2 MODIS satellite images

125 The MODIS sensor, onboard the TERRA - EOS/AM-1 satellite is acquiring near-daily images
126 of the Earth since February 25th, 2000. With 36 spectral bands ranging from 0.459 to 14.385
127 μm , and spatial resolution ranging from 0.25 to 1 km depending on the spectral band, MODIS



128 is nowadays one of the most used optical sensors for land surface observations. Because of its
 129 short temporal revisit time, its long acquisition period and its moderate resolution, images
 130 from MODIS are the most suitable for the present work. We therefore rely on about 15,000
 131 MODIS calibrated Level 1B (L1B) swath images.

#	Name	Mask size [Pixel]	$b_a = P_1^a \bar{\alpha}_a^{min} + P_2^a$				$b_s = P_1^s \bar{\alpha}_s^{int} + P_2^b$				$b_w = P_1^w \bar{\alpha}_w^{int} + P_2^w$			
			r^2	$RMSE$	P_1^a	P_2^a	r^2	$RMSE$	P_1^s	P_2^s	r^2	$RMSE$	P_1^w	P_2^w
1	Tour	71	0.78	0.61	14.9	-7.8								
2	Argentière	111	0.74	0.39	16.8	-8.4	0.76	0.27	12.3	-10.1	0.88	0.13	3.5	-0.3
3	Taléfre	40	0.46	0.73	17.0	-8.0	0.46	0.69	15.9	-12.1	0.51	0.50	2.5	-0.5
4	Mer de Glace	246	0.16	0.89	8.7	-5.8	0.69	0.31	15.3	-12.1	0.90	0.14	12.6	-7.5
5	Tré la Tête	38	0.43	1.25	22.8	-10.0								
6	Savinaz	7	0.23	1.27	12.3	-7.4								
7	Gurraz	17	0.29	0.77	9.8	-5.8								
8	Sassière	19	0.52	0.67	8.2	-4.9								
9	Grande Motte	30	0.83	0.53	13.6	-6.5								
10	Mulinet	18	0.33	0.62	7.7	-4.5								
11	Grand Méan	11	0.44	0.64	7.8	-4.2								
12	Arcelin	37	0.64	0.52	6.6	-3.7								
13	Pelve	44	0.41	0.75	8.7	-5.7								
14	Arpont	41	0.28	1.0	9.8	-5.8								
15	Mahure	20	0.55	0.66	10.1	-5.1								
16	Vallonnet	19	0.36	0.66	3.4	-2.0								
17	Gébroulaz	23	0.62	0.45	9.1	-4.6	0.76	0.28	9.8	-7.9	0.36	0.19	1.6	-0.1
18	Baounet	11	0.16	0.64	2.8	-2.5								
19	Rochemelon	11	0.31	0.67	4.3	-2.8								
20	Saint-Sorlin	31	0.86	0.37	13.8	-6.3	0.94	0.21	14.7	-11.0	0.75	0.19	2.3	-0.5
21	Quirilies	15	0.60	0.54	11.4	-5.2								
22	Mont de Lans	35	0.69	0.64	11.4	-5.4								
23	Girose	60	0.70	0.43	9.1	-4.7								
24	Selle	13	0.79	0.41	9.0	-4.4								
25	Casset	7	0.73	0.47	8.9	-4.6								
26	Blanc	44	0.82	0.29	7.9	-3.9	0.72	0.26	9.2	-7.3	0.33	0.41	2.4	-0.9
27	Vallon Pilatte	7	0.68	0.56	16.0	-7.2								
28	Rouies	14	0.72	0.68	18.0	-7.8								
29	Sélé	12	0.63	0.61	10.9	-5.1								
30	Pilatte	18	0.68	0.83	28.1	-13.1								

132
 133 **Table 1:** List of studied glaciers, characteristics and albedo/mass balance correlations over
 134 2000-2015, except for seasonal coefficients (over 2000-2010). For localization, refer to Fig. 1.
 135 Highlighted rows exhibit glaciers where annual and seasonal in situ glacier-wide SMB data are
 136 available. The mask size is expressed in number of pixels. To obtain the glacier mask area in
 137 km^2 , one should multiply the mask size by $0.0625 km^2$. Determination coefficients are
 138 expressed for each glacier (full plotted results are shown in supplementary material). Note the
 139 units of r^2 (%), $RMSE$, P_1 and P_2 (*m w. e.*).

140
 141 **2.3 Surface mass balance data**

142 In the French Alps, six glaciers allow both the seasonal and annual analyses to be conducted,
 143 due to the availability of summer and winter SMB data (b_s and b_w , respectively) obtained from



144 in situ measurements with the glaciological method (unpublished data, LGGE internal report,
145 listed Table 1). Among them, glacier-wide annual SMB b_a of four glaciers (Argentière, Mer de
146 Glace, Gébroulaz and Saint-Sorlin glaciers) have also been calculated using the Lliboutry
147 approach (Lliboutry, 1974; Vincent, 2002; Vincent et al., 2000). The latter combines the
148 punctual in situ data and the glacier-wide surface elevation changes quantified from the
149 difference between DEM retrieved using aerial photogrammetry. In addition, glacier wide
150 annual SMB of the 30 studied glaciers were computed by Rabatel et al., 2016 using the end-
151 of-summer snow line measured on optical remote-sensing images and the glacier-wide mass
152 change quantified from DEMs differencing.

153 For the six glaciers where glacier-wide annual SMB are available from the two methods, i.e.,
154 in situ and satellite measurements, the average of the two estimates was used to calibrate and
155 evaluate the albedo method.

156 **2.4 In situ albedo measurements**

157 Albedo measurements acquired punctually using an AWS on Saint-Sorlin Glacier have been
158 used to evaluate the MODIS retrieved albedo. In situ albedo measurements were available for
159 three periods in the ablation zone (July-August 2006; June-August 2008; June-September
160 2009) and for one period in the accumulation zone (June-September 2008). Albedo data from
161 these AWS have been calculated as the ratio of the reflected to incident shortwave radiation
162 (0.3 to 2.8 μm) using two Kipp and Zonen pyranometers. With a potential tilt of the instrument
163 with respect to surface melting and the intrinsic sensor accuracy ($\pm 3\%$, Six et al., 2009), the
164 calculated albedo at the AWS shows a $\pm 10\%$ accuracy (Kipp and Zonen, 2009; Dumont et al.,
165 2012).

166 **3 Methods**

167 **3.1 MODImLab products**

168 MODIS L1B images were processed using the MODImLab toolbox (Sirguey, 2009). Image
169 fusion between MOD02QKM bands 1 and 2 at 250 m resolution and MOD02HKM bands 3 to
170 7 at 500 m resolution allows 7 spectral bands at 250 m resolution to be produced (Sirguey et



171 al., 2008). Then, atmospheric and topographic corrections are applied that include multiple
172 reflections due to steep surrounding topography (Sirguey, 2009). Various products are derived
173 from the corrected ground reflectance including snow and ice surface albedo (Dumont et al.,
174 2012). As recommended by Dumont et al. (2012) the WhiteSky (WS) albedo (estimated value
175 of the surface albedo under only diffuse illumination) is considered. The use of an anisotropic
176 reflection model for snow and ice has been preferred to the isotropic case, due to its closer
177 agreement with in situ measurements (Dumont et al., 2012). The MODImLab toolbox also
178 output sensor geometrical characteristics at the acquisition time such as the solar zenith angle
179 (SZA) and the observation zenith angle (OZA) used for post-processing the images (Sect. 3.4).
180 The MODImLab cloud detection algorithm is more conservative than the original MODIS
181 product (MOD35), and has been preferred as recommended in (Brun et al., 2015).
182 According to Dumont et al. (2012) and further assessed by (Sirguey et al., 2016) the overall
183 accuracy of MODImLab albedo product under clear-sky conditions is estimated at $\pm 10\%$.
184 To mitigate the impact of shadows over the glaciers, MODImLab uses a DEM from the
185 Shuttle Radar Topography Mission (SRTM – 90 m resolution – acquired in 2000) to estimate
186 the sky obstruction by the surrounding topography and to correct the impact of shadows (see
187 Sirguey et al., 2009). The algorithm implemented in MODImLab is fully described in (Sirguey
188 et al., 2009) and inspired from (Dozier et al., 1981; Dozier and Frew, 1990) for the sky
189 obstruction factor processing (Horizon and Vsky in Sirguey et al., 2016), and from (Richter,
190 1998) for correction of shadows. It is first computed at 125 m resolution, providing Boolean-
191 type products of self and cast shadows per pixel. Results are then averaged and aggregated to
192 250 m resolution, producing sub-pixel fraction of shadow (further detailed in Sirguey et al.,
193 2009). Finally, MODIS data processed with MODImLab provides, among others, near-daily
194 maps of white-sky albedo at 250 m resolution together with cloud masks and cast and
195 projected shadows.
196 Albedo maps have been processed for 5,068 images for the Ecrins range, 4,973 for Mont-
197 Blanc and 5,082 for Vanoise over the period 2000-2015. Only images acquired between 09h50



198 and 11h10 AM UTC (+1h in winter and +2h in summer for local time conversion) were
199 selected to get minimum SZA and limit projected shadows of surrounding reliefs.

200 **3.2 Glacier masks**

201 Following Dumont et al. (2012) and Brun et al. (2015), we manually created raster masks of
202 the 30 glaciers, based on the glaciers' outlines from 1985-87 (Rabatel et al., 2013) and high
203 spatial resolution (6 m) SPOT-6 images from 2014. All debris-covered areas, together with
204 mixed pixel (rock-snow/ice) have been removed to capture only the snow/ice albedo signal.

205 The resulting number of pixels per glacier is listed in Table 1.

206 **3.3 Surface albedo and glacier-wide mass balance relationship**

207 **3.3.1 Basis of the method**

208 For glacier in the Alps (Dumont et al., 2012), the Himalayas (Brun et al., 2015) and in the
209 Southern Alps of New Zealand (Sirguey et al., 2016), the summer minimum glacier-wide
210 averaged albedo ($\bar{\alpha}_a^{\min}$) has been significantly correlated to the glacier-wide annual SMB. This
211 relation allowed the glacier-wide annual SMB reconstruction from satellite images on the
212 Brewster Glacier, New Zealand, over the period 2000-2014 (Sirguey et al., 2016). The
213 relationship between $\bar{\alpha}_a^{\min}$ and glacier-wide SMB results from the fact that solar radiation is the
214 main source of energy for melting snow and ice, both at the surface and within the first
215 centimeters below the surface (Van As, 2011). But this is not sufficient to explain why
216 averaged surface albedo is suitable for monitoring glacier SMB.

217 If we consider a temperate glacier in the mid-latitudes, its surface is fully covered by snow in
218 winter, leading to high and uniform surface albedo ($\bar{\alpha} \approx 0.8$ in Cuffey and Paterson, 2010).
219 During the ablation season, the accumulation area is still covered with snow conversely to the
220 ablation area where the ice is exposed and sometimes covered by debris. The overall albedo of
221 the glacier surface is therefore decreasing over the course of the ablation season, providing
222 information on the ratio of these two areas. The ratio between the size of the accumulation
223 zone and the entire glacier, called the accumulation-area ratio (AAR) has often been used as a



224 predictor of SMB both qualitatively (LaChapelle, 1962; Meier and Post, 1962; Mercer, 1961)
 225 or quantitatively (Dyrgerov et al., 2009). Therefore, assessing $\bar{\alpha}_a^{\min}$ provides insights of the
 226 relative share between the exposed ice and the snow-covered areas at the end of the ablation
 227 season, also quantified by the AAR.

228 3.3.2 From annual to seasonal surface mass balances

229 In this study, $\bar{\alpha}_a^{\min}$ has been computed for the 30 glaciers in order to validate the method at a
 230 regional scale. $\bar{\alpha}_a^{\min}$ occurs in summer, minimums out of summer are most likely artifacts.
 231 Then, $\bar{\alpha}_a^{\min}$ has been directly correlated to available annual SMB data (listed in Table 1).
 232 Following the work by Sirguey et al. (2016) on Brewster Glacier, a similar approach has been
 233 used in order to validate the method at a seasonal scale but only on six glaciers (within our
 234 sample of 30) for which the seasonal SMB are available. Conversely to Sirguey et al. (2016),
 235 the summer SMB b_s has been compared to the integrated albedo signal $\bar{\alpha}_s^{\text{int}}$ during the entire
 236 ablation season (1st May to 30th September) computed as follow and illustrated in Fig. 2.

$$237 \quad \bar{\alpha}_s^{\text{int}} = \int_{05.01}^{09.30} \bar{\alpha}(t).dt \quad \text{Eq. (1)}$$

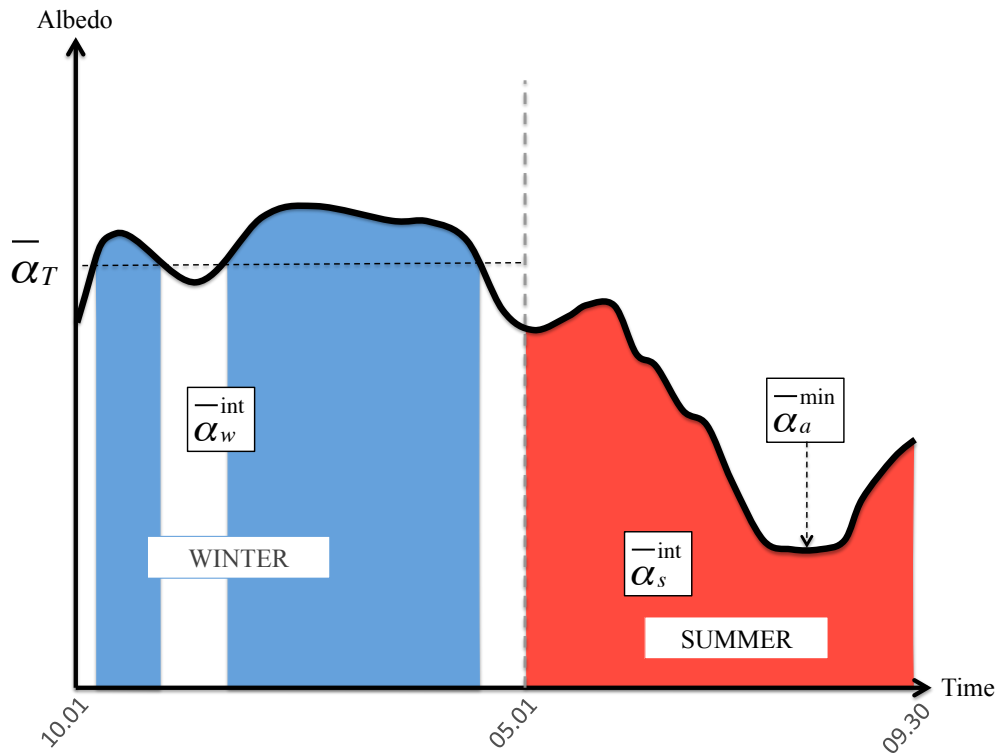
238
 239 For the winter period (1st October to 30th April), the albedo signal has been computed similarly
 240 than in Sirguey et al. (2016) by integrating the albedo when exceeding a threshold $\bar{\alpha}_r$,
 241 considered as representative of fresh snowfall events (illustrated by the blue shaded area in
 242 Fig. 2), as described by Eq. (2):

$$243 \quad \bar{\alpha}_w^{\text{int}} = \int \bar{\alpha}(t) \left\{ \begin{array}{l} \text{if } \bar{\alpha}(t) \text{ is found between } 10.01 \text{ and } 04.30 \\ \text{Only if } \bar{\alpha}(t) \geq \bar{\alpha}_r \end{array} \right. \quad \text{Eq. (2)}$$

244 The best threshold is the one maximizing the correlation between the retrieved cumulative
 245 winter albedo $\bar{\alpha}_w^{\text{int}}$ and the winter SMB. Threshold values have been computed independently
 246 for each of the six seasonally monitored glaciers. To evaluate the impact of this threshold $\bar{\alpha}_w^{\text{int}}$



247 has been computed without threshold over winter months (equivalent to $\bar{\alpha}_r = 0$). Finally,
 248 hundred thresholds ranging from 0 to 1 every 0.01 have been tested to assess the sensitivity of
 249 the method to $\bar{\alpha}_r$ (discussed Sect. 5). To compare each year together and remove the impact
 250 of the variable integration time period for each glacier, both $\bar{\alpha}_s^{\text{int}}$ and $\bar{\alpha}_w^{\text{int}}$ have been divided by
 251 the number of integrated days.
 252



253
 254 **Figure 2:** Schematic of a typical albedo cycle over one year, displaying parameters which
 255 have been linked to annual, summer (between 1st May and 30th September in the northern
 256 hemisphere) and winter (between 1st October and 30rd April in the northern hemisphere) SMB.
 257 $\bar{\alpha}_w^{\text{int}}, \bar{\alpha}_s^{\text{int}}$ are retrieved using Eq. (2) and Eq. (1) respectively. $\bar{\alpha}_T$ represents an example of
 258 threshold tested in Eq. (2). The summer minimum value of albedo is represented by $\bar{\alpha}_a^{\text{min}}$.

259



260 **3.4 Data filtering**

261 MODIS offers the opportunity to get daily images, but retrieving daily maps of Earth surface
262 albedo remains challenging. Indeed, various sources of error require filtering the available
263 images in order to only capture physical changes of the observed surface and not artifacts.
264 Clouds are known to be a major problem in optical remote sensing of the Earth surface
265 especially in the case of ice and snow covered surfaces. Even if some algorithms exist to
266 differentiate clouds and snow-covered areas (e.g., Ackerman et al., 1998; Sirguey et al., 2009),
267 omission errors are difficult to avoid, leading to erroneous albedo of the surface.

268 In this study, all images with a presence of cloud greater than 30% of the total glacier surface
269 area have been discarded. This threshold is higher than that chosen in Brun et al. (2015) on the
270 Chhota Shigri Glacier (20%), and we thus discuss Sect. 5.1 the impact of the computed cloud
271 threshold on the derived albedo results. When determining $\bar{\alpha}_a^{\min}$, 0% of cloud cover has been
272 imposed as a condition and visual check for each year and each glacier has been performed.
273 Snapshots from the fusion of MODIS bands 1 to 3 and from bands 4 to 6 (Sirguey et al., 2009)
274 have been used to visually check the images, together with images from other satellites
275 (mostly from the Landsat archive) and pictures and comments from mountaineering forums.
276 This last step, although laborious when studying 30 glaciers allowed the identification of the
277 summer minimum to be improved. Visual check of the images also confirms that projected
278 shadows of clouds are not affecting the albedo map. Another source of error is the impact of
279 the OZA. As mentioned in Sirguey et al. (2016), accuracy of the MODIS retrieved albedo
280 strongly decreases for viewing angles above 45° as pixel size increases from 2 to 5-folds from
281 OZA = 45° to 66° (Wolfe et al., 1998). This phenomenon is accentuated when observing
282 steep-sided snow/ice surfaces, surrounded by contrasted surfaces (rocks, forests, lakes...). This
283 distortion could lead to capture the mean albedo of a glacier plus its surroundings. Following
284 this, we decided to filter the images according to their OZA angle, as further described Sect.
285 4.1.

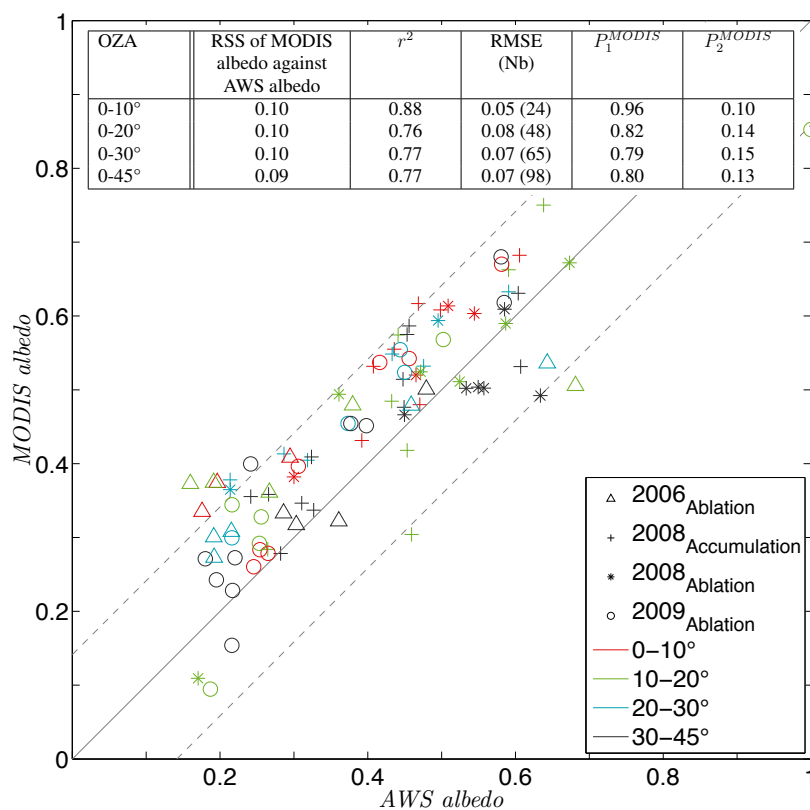


286 **4 Results**

287 **4.1 Retrieved albedo assessment**

288 A quantitative evaluation of the retrieved albedo has been performed with AWS deployed on
289 Saint-Sorlin Glacier. Measurements have been synchronized between punctual albedo for
290 MODIS and a 2-hour averaged albedo around MODIS acquisition time for the AWS. It is
291 worth reminding some differences between the in situ measured albedo data and the one
292 retrieved using MODIS. The downward facing pyranometer stands at around 1 m above the
293 surface, corresponding to a monitored footprint of *ca.* 300 m² (theoretical value for a flat
294 terrain) while the pixel area of MODIS products matches 62,500 m². Quantified albedos
295 from each method are therefore not representative of the same area. On the other hand,
296 incoming radiation data are extremely sensitive to a tilt of the sensor located on the AWS and
297 maintaining a constant angle throughout the monitoring period remains challenging, especially
298 during the ablation season. For instance, a tilt of 5° of the pyranometer at the summer solstice
299 can increase by 5% the error on the irradiance measurement (Bogren et al., 2016). No sensor
300 tilt was deployed on the AWS, thus preventing the application of tilt-correction methods (e.g.,
301 Wang et al., 2016). Nonetheless, regular visit allowed to maintain the sensor horizontal and to
302 limit errors in the irradiance measurements.

303



304

305 **Figure 3:** MODIS albedo and AWS albedo data for different OZA classes on Saint-Sorlin
 306 Glacier. Years indicated in the caption correspond to the year of acquisition while subscripts
 307 express the AWS location in the accumulation or ablation areas. The mean discrepancy
 308 between MODIS and AWS albedo per OZA is quantified by the RSS (residual sum of square).
 309 Correlation coefficient per OZA classes are also provided, with r^2 , RMSE together with the
 310 number of compared measurements (Nb), and coefficients of the equation:
 311 $MODIS_{albedo} = P_1^{MODIS} AWS_{albedo} + P_2^{MODIS}$. The continuous grey line illustrates the 1:1
 312 relationship between AWS and MODIS retrieved albedo. Thin and dotted lines represent the
 313 combined uncertainties on both AWS and MODIS retrieved albedo (absolute value of 10% for
 314 each), only accounting for intrinsic sensor accuracy and not for errors related to the acquisition
 315 context, e.g. size of the footprint.

316



317 Figure 3 illustrates the comparison between the retrieved and measured albedos at the AWS
318 locations for various OZA classes. One can note minor differences between the data plotted in
319 Fig. 3 and those presented in Dumont et al. (2012, Fig. 2). These differences are related to
320 changes in the MODImLab algorithm and different computation of the in situ albedo,
321 integrated over a two-hour period in the current study.

322 In Fig. 3, the spread between MODIS and AWS albedos is higher for low albedos (i.e. ablation
323 area). This is related to the footprint difference as described earlier, accentuating the albedo
324 differences when monitoring heterogeneous surface (snow patches, melt ponds...), even
325 more pronounced in summer. One can also note that MODIS albedo often over-estimate the
326 AWS albedo value. This over-estimation could be explained by: (1) the MODImLab albedo
327 retrieval algorithm. Indeed, under-estimation of the incoming radiation computed in the
328 MODImLab algorithm would lead to over-estimated retrieved albedo values, in addition the
329 atmospheric corrections used to compute the incident radiation could be hypothesized as
330 source of error (e.g. modeled transmittance through a simplified computed atmosphere, refer
331 to (Sirguey et al., 2009) for further description); (2) the AWS albedo measurements. Indeed,
332 view angles of AWS pyranometers (170°) could influence the retrieved albedo by monitoring
333 out-of-glacier features (e.g. moraines, rock walls, ...), resulting in under-estimated albedo
334 values. However, it is worth noting that most of the points are within the combined uncertainty
335 of both sensors and these differences in albedo retrieved from MODIS and the AWS are thus
336 hard to interpret.

337 Finally, Fig. 3 shows substantial differences between $OZA < 10^\circ$ and other OZA classes. For
338 $OZA < 10$, MODIS albedos better agree with AWS albedos than for the three other classes.
339 Integrating MODIS images with $OZA > 10^\circ$ substantially deteriorate the agreement with AWS
340 albedos (in term of r^2 , $RMSE$ and the slope P_I^{MODIS}), especially on "narrow" targets as alpine
341 mountain glaciers. We therefore chose to prioritize images acquired with low OZA to avoid
342 detection of non-glacierized surfaces. Therefore, four classes of images have been selected
343 following the criteria presented in Table 2.



Class	OZA (°)	Criteria
I	$OZA \leq 10$	All retained
II	$10 < OZA \leq 20$	Retained if more than 7 days between consecutive images from class I
III	$20 < OZA \leq 30$	Retained if more than 7 days between consecutive images from class I+II
IV	$OZA > 30$	Not retained

344

345

Table 2: Filtering the images from OZA values.

346

347 For the rest of the computation, the absolute $\pm 10\%$ accuracy per pixel estimated in Dumont et
 348 al. (2012) has been considered. We determined the uncertainty on $\bar{\alpha}$ by accounting for the
 349 spatial variability of the albedo signal within the glacier and considering that our sets of pixels
 350 are independent from each other (Eq. (3)):

351

$$\sigma_{\bar{\alpha}} = \frac{\sigma}{\sqrt{N}} \quad \text{Eq. (3)}$$

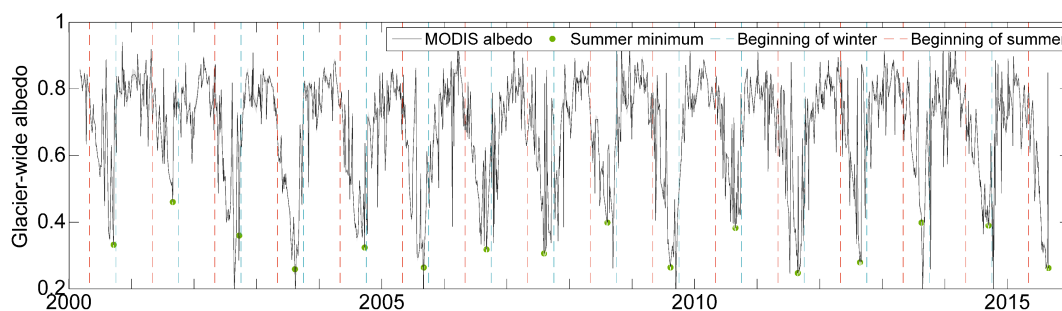
352

where σ stands for the standard deviation of the pixels albedo with N the number of pixels.

353 4.2 Temporal variability of the albedo signal

354

Using the "step-by-step" filtering procedure explained in Sect. 3.4, the ~ 16 -yr albedo cycle of
 355 each of the 30 glaciers was obtained (results available in the supplementary material). Figure 4
 356 illustrates the entire albedo time series for Saint-Sorlin Glacier over the period 2000-2015. We
 357 observed that the albedo decreases from the beginning of summer (dashed red line), reaching
 358 $\bar{\alpha}_a^{\min}$ in August/September and rising again at the end of September. This cyclicity is a proxy
 359 of surface processes. The snow cover decreases at the beginning of summer until reaching its
 360 lowest extent, and finally increases again with the first snowfall in late summer to reach its
 361 maximum extent in winter/spring.



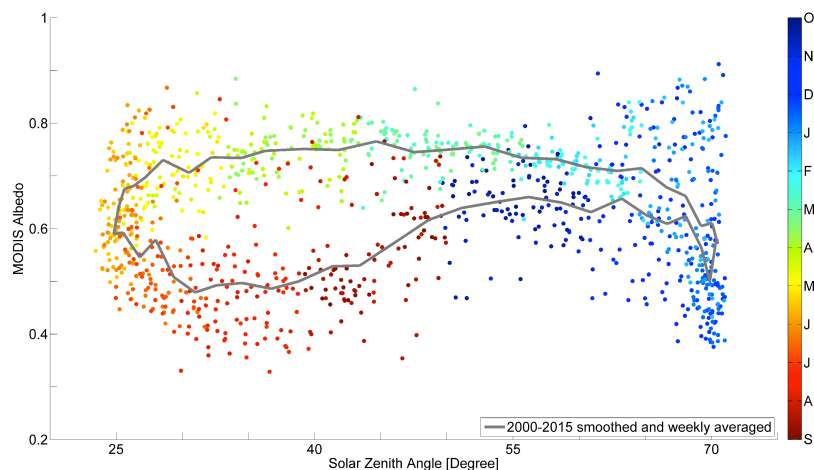
363 **Figure 4:** ~16-yr albedo course for Saint-Sorlin Glacier. Glacier-wide averaged albedo is
364 represented with the continuous black line. The green dots spot for each summer the minimum
365 average albedo, and have been manually checked for all years and glaciers. Dashed red and
366 blue lines stand for the beginning of the defined ablation and accumulation seasons (May and
367 October 1st respectively).

368

369 The periodicity of the albedo signal is however not so well defined for some of the studied
370 glaciers. For instance, Argentière Glacier exhibits a severe drop of $\bar{\alpha}$ in winter, reaching
371 values as low as summer minimums ($\bar{\alpha} \approx 0.4$). The observed drop of albedo in winter occurs
372 during more than one month centered on the winter solstice (December 21st) and is observed
373 for nine glaciers (Argentière, Baounet, Casset, Blanc, Girose, Pilatte, Vallon Pilatte, Tour and
374 Sélé glaciers, refers to supplementary material for full results). These glaciers are located
375 within the three studied mountain ranges but have the common characteristic to be very
376 incised with steep and high surrounding faces. We studied the albedo series as a function of
377 the SZA to reveal possible shadowing on the observed surfaces. Figure 5 displays the same
378 cycle as Fig. 4 for Argentière Glacier but providing information about SZA. As a reminder,
379 the MODImLab white-sky albedo is independent of the illumination geometry but the
380 computed albedo for each pixel can be subject to shadowing from the surrounding topography.
381 Two main observations stand out from the winter part of the cycle in Fig. 5: (i) most of
382 MODIS $\bar{\alpha}$ severely decrease under $\bar{\alpha} = 0.6$ for SZA greater than 60° corresponding to



383 November to January images, (ii) these drops are not systematic and we rather observe a
384 dispersion cone than a well-defined bias. As there are no physical meanings to systematic
385 change of the surface albedo during a part of the winter period and owing to the fact that this
386 dispersion is only observed for topographically incised glaciers, these decreases in albedo have
387 been considered as artifacts. These observations led us to carefully process winter albedos and
388 to perform a sensitivity study on the impact of the threshold albedo parameter $\bar{\alpha}_T$.



389
390 **Figure 5:** Albedo cycle for Argentière Glacier as a function of the SZA. Each point
391 corresponds to glacier-wide averaged albedo for each available image. The 16 years are
392 displayed. Color scale gives indication on the date of the used image. The thick grey line
393 describes the weekly albedo averaged over the entire study period. For readability purpose, the
394 averaged albedo has been smoothed, using a 7 points running average.

395

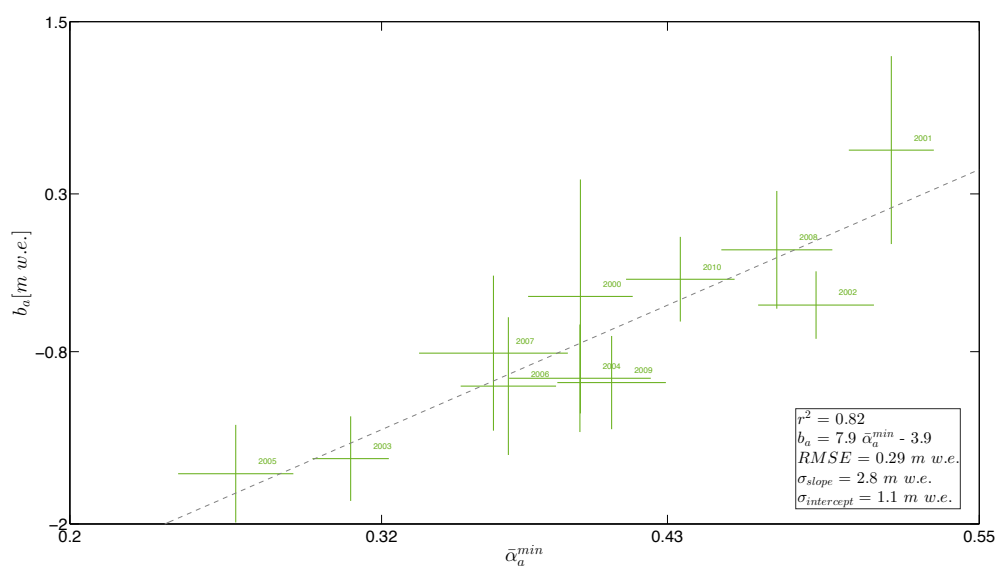
396 4.3 Albedo and glacier-wide surface mass balance

397 4.3.1 $\bar{\alpha}_a^{\min}$ and annual surface mass balance

398 The summer minimum average albedo for each year and each glacier has been linearly
399 correlated to the glacier-wide annual SMB. Figure 6 illustrates the relationship between $\bar{\alpha}_a^{\min}$



400 and b_a for Blanc Glacier (all the other glaciers are shown in the supplementary material). Error
 401 bars result from the dispersion of the SMB dataset for each year, and from the glacier intrinsic
 402 variability of the albedo signal the day of $\bar{\alpha}_a^{\min}$ acquisition. For the glaciers where the glacier-
 403 wide annual SMB is available from the SLA method, the uncertainty is about $\pm 22 \text{ cm w.e.}$ on
 404 average (ranging from 19 to 40 cm w.e. depending on the glacier, Rabatel et al., 2016).



405
 406 **Figure 6:** Annual SMB as a function of the MODIS retrieved summer minimum glacier-wide
 407 average albedo for Blanc Glacier. Error bars result on the dispersion of the available annual
 408 SMB data and on the quadratic sum of the systematic errors made on each albedo
 409 measurement. The thin dashed grey line illustrates the line of best fit, along with regression
 410 coefficients and significance.

411
 412 Twenty-seven glaciers show significant correlations (refer to Table 1 for full results) if
 413 considering a risk of error of 5% (according to a Student's t test). However, the linear
 414 correlation has no statistical significance for three glaciers with $r^2 < 0.25$. A possible
 415 explanation is the high number of removed images in summer due to manually checked thin
 416 overlying clouds not detected by the MODImLab cloud algorithm.

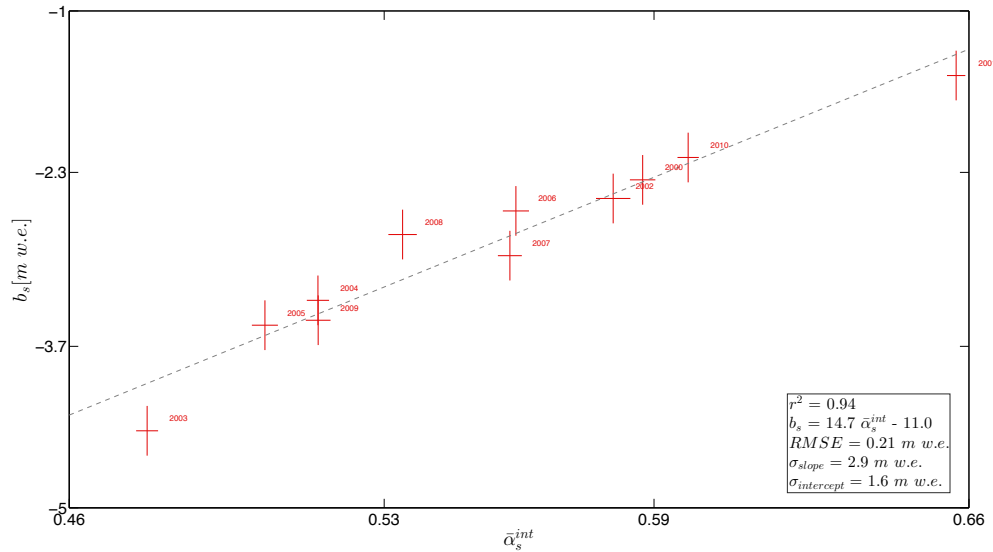


417 Looking at the 27 glaciers for which significant relationships have been found, 2001 is
418 regularly identified as an outlier. According to existing SMB datasets, 2001 is the only year of
419 the period 2000-2015 for which the annual SMB has been positive for all the studied glaciers
420 (0.80 m w.e. yr⁻¹ in average). Hence, according to computed determination coefficients in
421 Table 1, correctly predicting the surface mass balance values for the year 2001 using the
422 albedo method would imply to monitor a high value of minimum glacier-wide average albedo,
423 often greater than 0.7 (i.e. 0.83 and 0.95 for Rochemelon and Vallonnet glaciers, respectively).
424 Taking into consideration snow metamorphisms during the summer period, melting at the
425 surface and possible deposition of debris or dusts, monitoring such high albedo values
426 averaged at the glacier scale is unrealistic. Furthermore, removing 2001 from the time series
427 does not increase the number of glaciers for which the correlation is significant.

428 Finally, this study confirms the robust correlation between $\bar{\alpha}_a^{\text{min}}$ and b_a for 27 of the 30 studied
429 glaciers. It also reveals some limitations by under-estimating the annual SMB value for years
430 with very positive annual SMB.

431 **4.3.2 $\bar{\alpha}_s^{\text{int}}$ and summer surface mass balance**

432 Studying the integral of the albedo signal during the ablation season can provide insights on
433 the intensity of the ablation season and thus on the summer SMB b_s . As described in Sect.
434 3.3.2, $\bar{\alpha}_s^{\text{int}}$ has been computed and connected to the in situ b_s . Figure 7 illustrates the results
435 for Saint-Sorlin Glacier.



436

437 **Figure 7:** Summer SMB b_s expressed as a function of the integrated albedo over the entire
 438 ablation season for Saint-Sorlin Glacier. Error bars result from the uncertainties related to the
 439 glaciological method (measurements and interpolation at the glacier scale of the punctual
 440 measurements, ± 20 cm w.e. in total), and on the quadratic sum of the systematic errors made
 441 on each albedo measurement. Thin dashed grey line represents the linear regression showing
 442 the best correlation between the two variables, together with correlation coefficients.

443

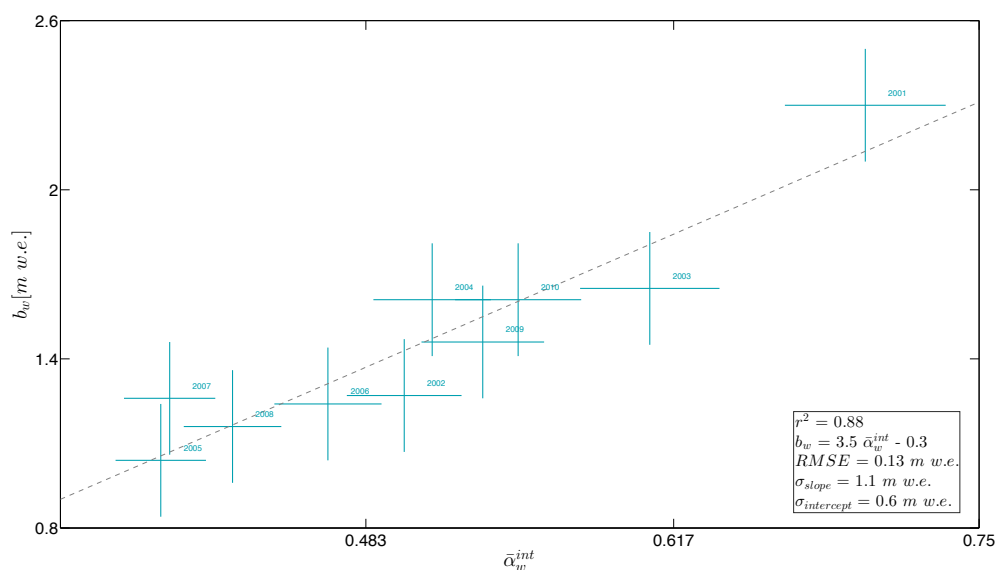
444 Saint-Sorlin Glacier, together with the five other seasonally surveyed glaciers showed a
 445 significant correlation between the two observed variables (from $r^2 = 0.46$ to $r^2 = 0.94$ with an
 446 error risk $< 5\%$, all statistics referred in Table 1). Conversely to $\bar{\alpha}_a^{\min}$, $\bar{\alpha}_s^{\text{int}}$ is slightly more
 447 robust to the presence of undetected clouds as its value does not rely on a single image. The
 448 lowest correlation has been found for Talèfre Glacier. The latter accounts for a relatively large
 449 debris-covered tongue that has been excluded when delineating the glacier mask (see
 450 supplementary material). Consequently, the low correlation could be partly explained by this
 451 missing area, considered in the glaciological method but not remotely sensed. To conclude,



452 $\bar{\alpha}_s^{int}$ has been significantly correlated to b_s and is therefore a reliable proxy to record the
 453 ablation season.

454 4.3.3 Retrieval of winter surface mass balance

455 As described Sect. 3.3.2, a similar method to the one used by Sirguey et al. (2016) has been
 456 applied for winter SMB quantification. Figure 8 illustrates the computed correlation for
 457 Argentière Glacier. Results for the five other seasonally investigated glaciers are listed in
 458 Table 3. The use of a glacier-dependent threshold value $\bar{\alpha}_r$ substantially improves the
 459 correlation between winter SMB and $\bar{\alpha}_w^{int}$ for three of the six glaciers (Saint-Sorlin, Blanc and
 460 Talèfre glaciers).



461
 462 **Figure 8:** Winter SMB, b_w , expressed as a function of the integrated albedo over the entire
 463 accumulation season for Argentière Glacier. Winter SMB of 2001 corresponds to the winter
 464 2000/2001. Error bars result from the uncertainties related to the glaciological method and on
 465 the quadratic sum of the systematic errors made on each albedo measurement. Thin dashed
 466 grey line represents the linear regression showing the best correlation between the two
 467 variables, together with correlation coefficients.

468



469 For Argentière, Mer de Glace and Gébroulaz glaciers, a significant correlation is found
470 whatever the value of the albedo threshold $\bar{\alpha}_T$ is (Table 3). Furthermore, $\bar{\alpha}_T$ is far from being
471 uniform on the six glaciers ($0.53 \geq \bar{\alpha}_T \geq 0.76$). We therefore reconsider the idea of using a
472 threshold as a representative value of fresh snowfall, as there is no physical reason that this
473 threshold varies, at least within the same region.

Glacier	$\bar{\alpha}_T$	r^2 using $\bar{\alpha}_T$	r^2 without $\bar{\alpha}_T$
Saint-Sorlin	0.76	0.75	0.21
Argentière	0.58	0.88	0.76
Talèfre	0.68	0.59	0.25
Mer de Glace	0.53	0.90	0.87
Gébroulaz	0.75	0.36	0.25
Blanc	0.70	0.33	0.21

474

475 **Table 3:** Coefficients of determination for the relationship between the winter SMB b_w and the
476 integrated winter albedo, computed with and without the albedo threshold $\bar{\alpha}_T$.

477

478 5 Discussion

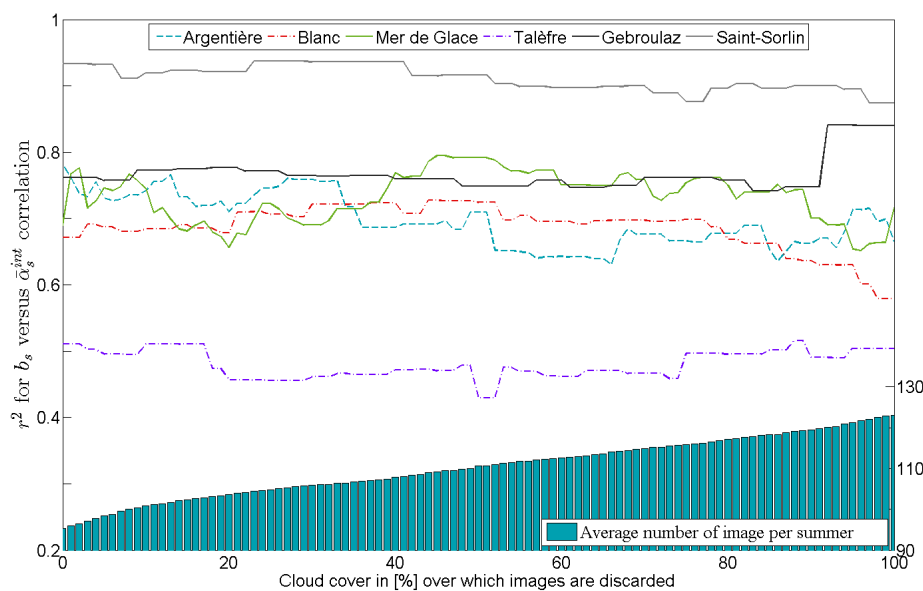
479 In this section, we first discuss the impact of the threshold applied to the cloud cover fraction
480 on the obtained results. Then, the observed discrepancies and artifacts of the winter albedo
481 signal on some of the studied glaciers have been analyzed through a sensitivity study focused
482 on the algorithm correcting the shadows. Afterward, we discuss the sensitivity of the
483 correlation, between $\bar{\alpha}_w^{\text{int}}$ and b_w , toward the selected albedo threshold $\bar{\alpha}_T$. We finally express
484 the main limitations and assessments of the albedo method.

485 5.1 Cloud coverage threshold

486 As stated in Sect. 3.4, a value of 30% of cloud coverage over the glacier mask has been
487 defined as the acceptable maximum value for considering the albedo map of the day. We
488 computed a sensitivity study on the impact of this threshold on the value of the obtained
489 correlations between the integrated summer albedo and the in situ summer SMB. The summer
490 period has been chosen as it represents the period when the albedo of the glacier is the most



491 contrasted, between bare ice and snow/firn. The glacier-wide average albedo in this period is
492 therefore more sensitive to possible shading of a part of the glacier. Figure 9 illustrates the
493 results for the six seasonally surveyed glaciers. The used value of the allowed cloud coverage
494 appears not to have a substantial impact on the correlation. This observation first implies that
495 the MODImLab cloud product is reliable enough to only compute surface albedo and to avoid
496 too frequent misclassification between the clouds and the surface. It also suggests that
497 removing too many images because of partial cloud cover removes information about the
498 glacier-wide average albedo variability. However, allowing all images, even when the glacier-
499 wide average albedo is computed on only 10% of the glacier (90% of detected cloud
500 coverage), does not reduce significantly the correlation for most of the six glaciers.



501
502 **Figure 9:** r^2 for the six seasonally surveyed glaciers for the albedo summer integral *versus*
503 summer SMB relationship against the cloud threshold above which images have been
504 discarded during the summer season. For the computation, hundred thresholds have been
505 tested between 0 and 100%. The inner histogram illustrates the number of considered images
506 per summer and averaged on the six glaciers.



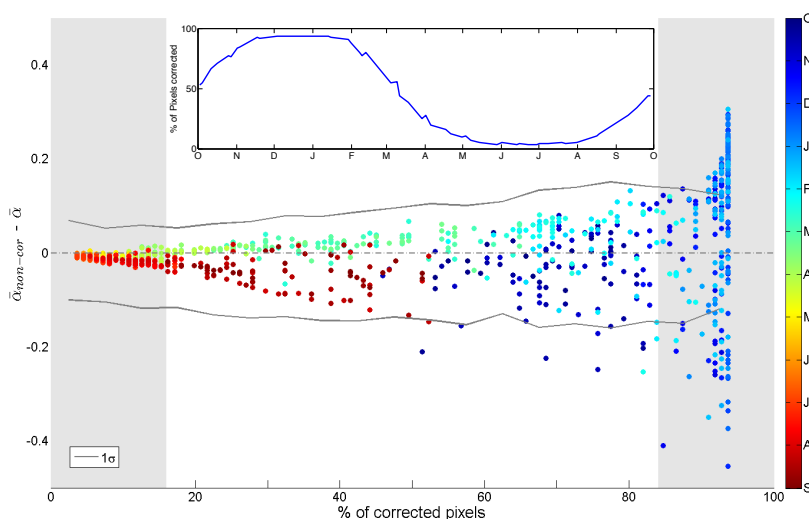
507
508 Nevertheless, hypothesizing that the glacier-wide average albedo of a small fraction of the
509 glacier (e.g., 10%) is suitable to represent the entire glacierized surface is questionable. It
510 therefore depends on the size of the observed glacier, where 10% of a glacier of 3 and 30 km²
511 have not the same meaning, but also on the delineated mask (ablation area not entirely
512 considered because of debris coverage...). The summer-integrated albedo is also highly
513 dependent on the time gap between useful images. In other words, if an image has an
514 "anomalous" glacier-wide average albedo because of high cloud coverage, the impact on the
515 integrated value will be smaller if "normal condition" albedos are monitored at nearby dates.
516 The average number of available images per year does not largely differ between the various
517 computed cloud coverage thresholds. It varies in average from 95 to 123 images per summer
518 period for respectively 0% and 100% cloud coverage threshold. Intermediate values are 106,
519 111 and 116 images per summer for 30, 50 and 75% cloud coverage threshold, respectively.
520 The difference in significance of r^2 (according to a Student's t test) between opting for 0% and
521 100% is almost negligible, and choosing the best cloud threshold value is rather a compromise
522 between the number of used images and the resulting correlation with glacier-wide SMB. We
523 finally concluded that selecting cloud coverage threshold to 30% presents the best
524 determination coefficients between the integrated summer albedo and the summer balance for
525 most of the six glaciers without losing too much temporal resolution.

526 **5.2 Evaluation of winter albedo values**

527 In light of the documented dispersion on $\bar{\alpha}$ during some of the winter months on several
528 studied glaciers (Sect. 4.2), sensitivity of the MODIS retrieved albedo against correction of
529 shadows had been assessed. This work has only been conducted on the 250 m resolution raster
530 products and specifically on the cast shadow product because self-shadow corrections can be
531 considered as reliable enough because only related to the DEM accuracy. We thus defined a
532 pixel as "corrected" when at least one of its sub-pixels was classified as shadowed. From then
533 on, two glacier-wide albedos $\bar{\alpha}$ have been defined: (i) $\bar{\alpha}_{\text{non-cor}}$ computed on non-corrected



534 pixels only, classified as non-shadowed; (ii) $\bar{\alpha}$ of both corrected and non-corrected pixels,
535 equal to the glacier-wide average albedo. Figure 10 illustrates the difference between $\bar{\alpha}_{\text{non-cor}}$
536 and $\bar{\alpha}$ as a function of the percentage of corrected pixels over the entire glacier. The study
537 was performed on Argentière Glacier (111 pixels) that exhibited large $\bar{\alpha}$ artifacts in winter
538 (Fig. 5). The inner diagram allows emphasizing the annual “cycle” of modeled shadows,
539 contrasted between nearly no cast shadows in summer and an almost fully shadowed surface
540 in winter. We represent the 1 standard deviation of $\bar{\alpha}$, averaged by classes of 5% corrected
541 pixels. In other words, it illustrates the mean variability of the glacier-wide surface albedo.
542 Therefore, for images with $\bar{\alpha}_{\text{non-cor}} - \bar{\alpha}$ within the interval defined by 1 st.dev. of $\bar{\alpha}$, errors
543 resulting from the correction algorithm are smaller than the spatial variability of the glacier-
544 wide albedo glacier. We also selected only significant values, following a normal distribution
545 of the averaged $\bar{\alpha}$. Consequently, only values at $\pm 1\sigma$ (68.2%) in term of percentage of
546 corrected pixel have been retained (i.e. when the relative share of corrected pixels ranged from
547 15.9 to 84.1%). Between 0 and 15.9%, $\bar{\alpha}_{\text{non-cor}}$ and $\bar{\alpha}$ are not sufficiently independent
548 because of low number of corrected pixels, and beyond 84.1%, $\bar{\alpha}_{\text{non-cor}}$ is computed over a too
549 small number of pixels. As a consequence, even if the albedo correction in the shadowed parts
550 of the glacier could be improved, most of the errors related to this correction do not depreciate
551 the results. Above 80% of corrected pixels (December to early February), differences between
552 $\bar{\alpha}_{\text{non-cor}}$ and $\bar{\alpha}$ exceed the monitored spatial variability of $\bar{\alpha}$. These anomalies are at the root
553 of the observed artifacts Fig. 5 by the severe drops of albedos and described Sect. 4.2.



554

555 **Figure 10:** Impact of the ratio of corrected pixels toward the difference between non-corrected
 556 and glacier-wide albedo. Each point corresponds to one acquisition and the 16 years are
 557 therefore displayed on this graph. Color scale gives indication on the date of the acquired
 558 image. Grey shaded areas correspond to ratios of corrected pixels for which $\bar{\alpha}_{\text{non-cor}} - \bar{\alpha}$ has
 559 low statistical robustness (refer to the main text). Thin grey lines represent 1σ standard
 560 deviation of $\bar{\alpha}$, averaged by classes of 5% corrected pixels. The inner graph illustrates the
 561 amount of corrected pixel, function of the selected month.

562

563 In addition, a seasonality in the albedo signal can be observed with $\bar{\alpha}_{\text{non-cor}} - \bar{\alpha} > 0$ in early
 564 spring (February to April) while $\bar{\alpha}_{\text{non-cor}} - \bar{\alpha} < 0$ in summer and autumn (June to November).
 565 This could be explained by different localizations of shadowed area for a given ratio of
 566 corrected pixel. As an example, a glacier could have in October a snow- and shadow-free
 567 snout and a covered by fresh snow and shadowed upper section. This configuration would
 568 induce a negative difference as we observe from June to November. Conversely, this glacier
 569 could present in March (same ratio of corrected pixels than October) a complete snow



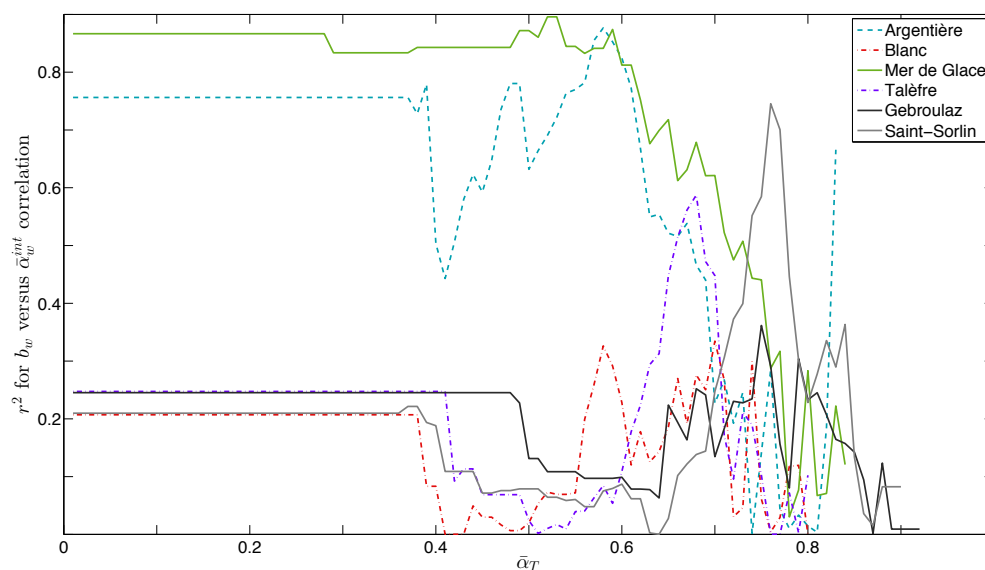
570 coverage, leading to a smaller difference between $\bar{\alpha}_{\text{non-cor}}$ and $\bar{\alpha}$ (<0.1) that could even result
571 on positive difference as we observe from February to April.
572 Finally, observed albedo artifacts in winter are most likely due to the correction of shadows.
573 On the other hand, correcting shadows accurately and consistently is extremely challenging.
574 As illustrated by Fig. 10, a way to confidently consider the albedo signal is to exclude values
575 with too large share of corrected pixels. However, because of the inter-annual approach carried
576 out in this study, such systematic artifact is not depreciating the results but would be a major
577 issue on studies focused on albedo values themselves (e.g. maps of snow extents...).

578 **5.3 Evaluation of the winter albedo threshold**

579 The albedo threshold, $\bar{\alpha}_T$, for which the winter albedo signal is integrated is considered in
580 Sirguey et al. (2016) as representative of the presence of fresh snow at the glacier surface. In
581 order to study the impact of $\bar{\alpha}_T$ on the correlation between the winter integrated albedo and
582 the in situ winter SMB, we computed the r^2 considering 100 values of $\bar{\alpha}_T$ (from 0 to 1).
583 Figure 11 displays the computed results for the six seasonally surveyed glaciers. No glacier
584 provides the same threshold maximizing r^2 . For Argentière and Mer de Glace, using a
585 threshold does not drastically maximize the relation and the integral can be processed without
586 using a threshold. These two glaciers also provide the best correlation coefficients compared
587 to the other four glaciers and are by far the largest glaciers of our monitoring set (14.59 and
588 23.45 km² for Argentière and Mer de Glace glaciers respectively). Indeed, a possible
589 explanation of this good correlation, even without threshold, relies on the morpho-topographic
590 features on these two large glaciers. With a glacier snout reaching 1600 m a.s.l., the tongue of
591 these glaciers can experience melting events (resulting in contrasted pixels in terms of albedo
592 value), even during the winter season. The glacier-wide albedo therefore provides a good
593 proxy of the winter SMB on the glacier because of the large altitudinal range of the glacier.
594 For Saint-Sorlin Glacier, a threshold of 0.76 improves significantly the correlation, similarly to
595 the threshold found for Brewster Glacier by Sirguey et al. (2016). We can mention the analogy



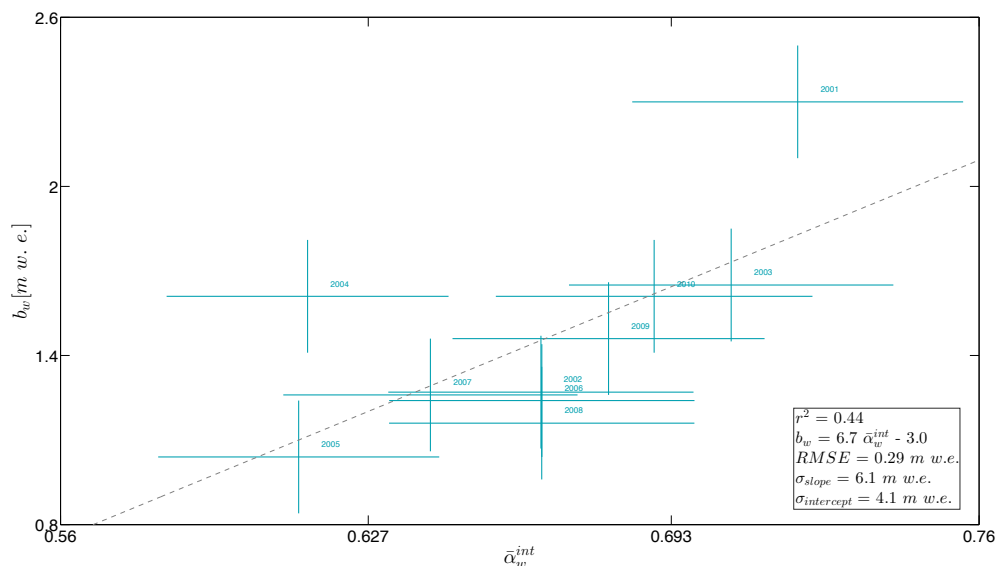
596 between Saint-Sorlin and Brewster, having similar morpho-topographic features, in terms of
 597 surface area, general aspect and slope. Talèfre Glacier, with $\bar{\alpha}_r$ equals 0.68, is the second
 598 glacier for which using a threshold significantly improves the correlation.



599
 600 **Figure 11:** r^2 of the albedo winter integral *versus* winter SMB relationship as a function of $\bar{\alpha}_r$
 601 chosen for the winter integration for the six seasonally monitored glaciers. Hundred thresholds
 602 have been tested between 0 and 1.
 603
 604 Nevertheless, all studied glaciers, apart from Mer de Glace, present a low robustness against
 605 $\bar{\alpha}_r$ and important and non-physical variations of r^2 occur for most of the computed $\bar{\alpha}_r$. The
 606 method is preferentially filtering years with repeated low albedos. Therefore, for a given
 607 threshold $\bar{\alpha}_r$, some years are necessarily more filtered than others resulting in large
 608 degradation or enhancement of the b_w vs. $\bar{\alpha}_w^{\text{int}}$ correlation. As an example for Argentière
 609 Glacier (Fig. 8 and Fig. 12 with $\bar{\alpha}_r$ equals 0.58 and 0.42 respectively), opting for $\bar{\alpha}_r=0.42$
 610 affecting preferentially years 2001 and 2004 and therefore reduces significantly the



611 correlation. On the other hand, given threshold can by chance, favors the b_w vs. $\bar{\alpha}_w^{\text{int}}$
 612 correlation.



613
 614 **Figure 12:** Similar relationship between b_w vs. $\bar{\alpha}_w^{\text{int}}$ but for $\bar{\alpha}_r = 0.42$. Axis, legend and
 615 uncertainties are identical to Fig.8.

616
 617 These results finally question the use of $\bar{\alpha}_r$ as a threshold detecting only fresh snowfall events
 618 and seems to maximize artificially the correlation between b_w and $\bar{\alpha}_w^{\text{int}}$. Large glaciers (>10
 619 km²) appear to be more robust for threshold-free detection but further studies on a more
 620 exhaustive set of large glaciers would be required.

621 5.4 Limits of the albedo method

622 In agreement with Dumont et al. (2012) and Brun et al. (2015), retrieving the glacier annual
 623 SMB from albedo summer minimums proves to be an efficient method. Low correlations often
 624 result from high and persistent cloud coverage during summer, reducing the chance of spotting
 625 the albedo summer minimum. For SMB reconstruction purpose, a future line of research could
 626 rest upon linking morpho-topographic features of the glacier such as glacier surface area,
 627 mean altitude or slope to the regression coefficients of both annual and seasonal SMB vs.



628 albedo relationships, giving the opportunity to establish analogy between monitored and
629 unmonitored glaciers. Tests have been carried out but no significant and satisfying results have
630 been obtained, due to a presumably too heterogeneous data set, where large glaciers ($>10 \text{ km}^2$)
631 and/or south-facing glaciers are largely under-represented. Larger scale studies and multi-
632 variable correlations in between morpho-topographic features could be for instance envisaged.
633 Using the albedo method at a seasonal scale has shown promising results, especially for the
634 summer period where significant correlations have been found for the six seasonally
635 monitored glaciers. There is still in this approach a step to retrieve the seasonal SMB of an
636 unmonitored glacier with high confidence. The winter season has shown results that are for
637 now not entirely satisfactory. Glaciers that experience complete snow coverage during most of
638 the winter season showed the lowest correlation ($r^2 \leq 0.33$) while the two glaciers showing the
639 best correlations are subject to some events of surface melting in their lower reaches,
640 particularly at the end of the winter season. Therefore, studying the albedo signal in winter
641 could record snowfall events but seems to be little sensitive to snowfall intensity.

642 An additional approach has been carried out, aiming at retrieving b_w by deduction from the
643 reconstructed b_a and b_s from the albedo signal. This approach, not using the winter albedo
644 signal, is poorly correlated ($r^2 < 0.16$) to in situ b_w for the six seasonally monitored glaciers.
645 Indeed, the result extremely depends on the quality of the correlations between b_a , b_s and the
646 albedo signals. Saint-Sorlin Glacier is a good example, being one of the glaciers with the
647 highest correlations for the annual ($r^2 = 0.86$) and summer ($r^2 = 0.94$) SMB. Subtracting b_s
648 from b_a to computed b_w leads to an average difference between computed and measured b_w of
649 $\pm 0.41 \text{ m w.e}$ for the 10 simulated years. As a consequence, in case of low correlations between
650 SMB and albedo, errors in the computed winter SMB become exacerbated.

651 **6 Conclusion**

652 In this study, we used the so-called albedo method to correlate annual and seasonal SMB to
653 glacier-wide average albedos obtained from MODIS images. This method has been carried on
654 30 glaciers located in the French Alps, over the period 2000-2015. Images processing has been



655 performed using the MODImLab algorithm, and filters on the images have been applied,
656 removing images with more than 30% cloud coverage, and excluding images with satellite
657 observation angles greater than 30°. Quality assessment has been performed and close
658 agreement has been found between albedos from AWS installed on Glacier de Saint-Sorlin
659 and MODIS retrieved albedo values. Annual SMB have been significantly correlated to the
660 summer minimum albedo for 27 of the 30 selected glaciers, confirming this variable as a good
661 proxy of the glacier-wide annual SMB. For the six seasonally monitored glaciers, summer
662 SMB obtained from the glaciological method have been significantly linked to the integral of
663 the summer albedo. For the winter season, implementing an albedo threshold for computing
664 the winter integral of the albedo has substantially improved the determination coefficients but
665 no uniform threshold has been found for the six selected glaciers. Two small glaciers, Saint-
666 Sorlin and Talèfre presented high correlation using albedo threshold, providing the
667 opportunity to reconstruct missing years or extending time series of these glaciers. Good
668 results have been obtained without using albedo thresholds in winter for Argentière and Mer
669 de Glace glaciers (>10 km²) and further study would be required on a more exhaustive set of
670 large glaciers. We hence reconsider the idea proposed by Sirguey et al. (2016) of using albedo
671 thresholds to detect snow falls covering the glacier surface but albedo thresholds seem to
672 maximize artificially the correlation between winter SMB and winter integrated surface
673 albedo.

674 Sensitivity study on the impact of the considered cloud coverage has revealed a high
675 confidence in the MODImLab cloud algorithm, limiting pixel misclassifications, and a rather
676 high tolerance of the integrated signal to the number of partly cloud-covered images. This
677 confidence on cloud filters is very promising to document unmonitored glaciers. Correction of
678 shadows by the MODImLab algorithm has however revealed some limitations when a large
679 share of the glacier is shadowed by the surrounding topography (around winter solstice).
680 Despite this, glacier with severe and artificial drops of albedo in winter performed well when
681 quantifying the winter SMB (e.g. Argentière Glacier). Such systematic errors are therefore not



682 an issue for inter-annual studies, but would be a serious issue on studies focused on albedo
683 values themselves.

684 Using optical satellite images to estimate glacier surface processes and quantify annual and
685 seasonal SMB from the albedo cycle is therefore very promising and should be expanded to
686 further regions. Using images from different satellites, combining high spatial and temporal
687 resolution instruments, could substantially reduces uncertainties, especially for spotting the
688 albedo summer minimum with more confidence, but also to improve the temporal resolution.
689 This method could then in the short term, become reliable for retrieving SMB of monitored
690 and unmonitored glaciers.

691

692 **Acknowledgment**

693 This study was conducted within the *Service National d'Observation* GLACIOCLIM. Equipex
694 GEOSUD (*Investissements d'avenir* - ANR-10-EQPX-20) is acknowledged for providing the
695 2014 SPOT-6 images. The MODIS Level-1B data were processed by the MODIS Adaptive
696 Processing System (MODAPS) and the Goddard Distributed Active Archive Center (DAAC)
697 and are archived and distributed by the Goddard DAAC. In situ mass balance data for the
698 Glacier Blanc were kindly provided by the *Parc National des Ecrins*. The authors
699 acknowledge the contribution the Labex OSUG@2020 (*Investissements d'avenir* – ANR10
700 LABX56). Pascal Sirguy thanks the University of Grenoble Alpes and Grenoble-INP for the
701 6-month “invited professor grant” obtained in 2015-16.

702



703 REFERENCES

- 704 Ackerman, S. A., Strabala, K. I., Menzel, W. P., Frey, R. A., Moeller, C. C. and Gumley, L. E.:
705 Discriminating clear sky from clouds with MODIS, *J. Geophys. Res. Atmospheres*, 103(D24), 32141–
706 32157, doi:10.1029/1998JD200032, 1998.
- 707 Berthier, E., Cabot, V., Vincent, C. and Six, D.: Decadal Region-Wide and Glacier-Wide Mass
708 Balances Derived from Multi-Temporal ASTER Satellite Digital Elevation Models. Validation over the
709 Mont-Blanc Area, *Front. Earth Sci.*, 4, doi:10.3389/feart.2016.00063, 2016.
- 710 Bogren, W. S., Burkhart, J. F. and Kylling, A.: Tilt error in cryospheric surface radiation measurements
711 at high latitudes: a model study, *The Cryosphere*, 10(2), 613–622, doi:10.5194/tc-10-613-2016, 2016.
- 712 Brun, F., Dumont, M., Wagnon, P., Berthier, E., Azam, M. F., Shea, J. M., Sirguey, P., Rabatel, A. and
713 Ramanathan, A.: Seasonal changes in surface albedo of Himalayan glaciers from MODIS data and
714 links with the annual mass balance, *The Cryosphere*, 9(1), 341–355, doi:10.5194/tc-9-341-2015, 2015.
- 715 Chen, J. and Ohmura, A.: Estimation of Alpine glacier water resources and their change since the
716 1870s, *IAHS Publ.*, 193, 127–135, 1990.
- 717 Church, J. A., Clark, P. U., Cazenave, A., Gregory, J. M., Jevrejeva, S., Levermann, A., Merrifield, M.,
718 Milne, G., Nerem, R., Nunn, P. and others: Sea level change, *Clim. Change 2013 Phys. Sci. Basis*
719 *Work. Group Contrib. Fifth Assess. Rep. Intergov. Panel Clim. Change*, 1137–1216,
720 doi:10.1088/1748-9326/8/1/014051, 2013.
- 721 Cuffey, K. M. and Paterson, W. S. B.: *The Physics of Glaciers*, Elsevier Science. [online] Available
722 from: <https://books.google.fr/books?id=Jca2v1u1EKEC>, 2010.
- 723 Dozier, J. and Frew, J.: Rapid calculation of terrain parameters for radiation modeling from digital
724 elevation data, *IEEE Trans. Geosci. Remote Sens.*, 28(5), 963–969, doi:10.1109/36.58986, 1990.
- 725 Dozier, J., Bruno, J. and Downey, P.: A faster solution to the horizon problem, *Comput. Geosci.*, 7,
726 145–151, doi:10.1016/0098-3004(81)90026-1, 1981.
- 727 Drolon, V., Maisongrande, P., Berthier, E., Swinnen, E. and Huss, M.: Monitoring of seasonal glacier
728 mass balance over the European Alps using low-resolution optical satellite images, *J. Glaciol.*, 62(235),
729 912–927, doi:10.1017/jog.2016.78, 2016.
- 730 Dumont, M., Gardelle, J., Sirguey, P., Guillot, A., Six, D., Rabatel, A. and Arnaud, Y.: Linking glacier
731 annual mass balance and glacier albedo retrieved from MODIS data, *The Cryosphere*, 6(6), 1527–
732 1539, doi:10.5194/tc-6-1527-2012, 2012.
- 733 Dyurgerov, M., Meier, M. F. and Bahr, D. B.: A new index of glacier area change: a tool for glacier
734 monitoring, *J. Glaciol.*, 55(192), 710–716, doi:10.3189/002214309789471030, 2009.
- 735 Gardelle, J., Berthier, E., Arnaud, Y. and Kääb, A.: Region-wide glacier mass balances over the Pamir-
736 Karakoram-Himalaya during 1999–2011, *The Cryosphere*, 7(4), 1263–1286, doi:10.5194/tc-7-1263-
737 2013, 2013.
- 738 Gardent, M., Rabatel, A., Dedieu, J.-P. and Deline, P.: Multitemporal glacier inventory of the French
739 Alps from the late 1960s to the late 2000s, *Glob. Planet. Change*, 120, 24–37,
740 doi:10.1016/j.gloplacha.2014.05.004, 2014.
- 741 Immerzeel, W. W., Beek, L. P. H. van and Bierkens, M. F. P.: Climate Change Will Affect the Asian
742 Water Towers, *Science*, 328(5984), 1382–1385, doi:10.1126/science.1183188, 2010.



- 743 Käab, A., Treichler, D., Nuth, C. and Berthier, E.: Brief Communication: Contending estimates of
744 2003–2008 glacier mass balance over the Pamir–Karakoram–Himalaya, *The Cryosphere*, 9(2), 557–
745 564, doi:10.5194/tc-9-557-2015, 2015.
- 746 Kaser, G., Grosshauser, M. and Marzeion, B.: Contribution potential of glaciers to water availability in
747 different climate regimes, *Proc. Natl. Acad. Sci.*, 107, 20223–20227, doi:10.1073/pnas.1008162107,
748 2010.
- 749 Kipp and Zonen: Instruction Manuel CNR1 Net radiometer, 2009.
- 750 LaChapelle, E.: Assessing glacier mass budgets by reconnaissance aerial photography, *J. Glaciol.*, 4,
751 290–297, 1962.
- 752 Lliboutry, L.: Multivariate Statistical Analysis of Glacier Annual Balances, *J. Glaciol.*, 13(69), 371–
753 392, doi:10.1017/S0022143000023169, 1974.
- 754 Meier, M. F. and Post, A.: Recent variations in mass net budgets of glaciers in western North America,
755 *IASH Publ*, 58, 63–77, 1962.
- 756 Mercer, J. H.: The Response of Fjord Glaciers to Changes in the Firn Limit, *J. Glaciol.*, 3(29), 850–
757 858, doi:10.1017/S0022143000027222, 1961.
- 758 Ohmura, A.: Cryosphere during the twentieth century, *Wash. DC Am. Geophys. Union Geophys.*
759 *Monogr. Ser.*, 150, 239–257, doi:10.1029/150GM19, 2004.
- 760 Pfeffer, W. T., Arendt, A. A., Bliss, A., Bolch, T., Cogley, J. G., Gardner, A. S., Hagen, J.-O., Hock,
761 R., Kaser, G., Kienholz, C., Miles, E. S., Moholdt, G., Mölg, N., Paul, F., Radić, V., Rastner, P., Raup,
762 B. H., Rich, J. and Sharp, M. J.: The Randolph Glacier Inventory: a globally complete inventory of
763 glaciers, *J. Glaciol.*, 60(221), 537–552, doi:10.3189/2014JoG13J176, 2014.
- 764 Rabatel, A., Dedieu, J.-P. and Vincent, C.: Using remote-sensing data to determine equilibrium-line
765 altitude and mass-balance time series: validation on three French glaciers, 1994–2002, *J. Glaciol.*,
766 51(175), 539–546, doi:10.3189/172756505781829106, 2005.
- 767 Rabatel, A., Dedieu, J.-P., Thibert, E., Letréguilly, A. and Vincent, C.: 25 years (1981–2005) of
768 equilibrium-line altitude and mass-balance reconstruction on Glacier Blanc, French Alps, using
769 remote-sensing methods and meteorological data, *J. Glaciol.*, 54(185), 307–314,
770 doi:10.3189/002214308784886063, 2008.
- 771 Rabatel, A., Letréguilly, A., Dedieu, J.-P. and Eckert, N.: Changes in glacier equilibrium-line altitude
772 in the western Alps from 1984 to 2010: evaluation by remote sensing and modeling of the morpho-
773 topographic and climate controls, *The Cryosphere*, 7(5), 1455–1471, doi:10.5194/tc-7-1455-2013,
774 2013.
- 775 Rabatel, A., Dedieu, J. P. and Vincent, C.: Spatio-temporal changes in glacier-wide mass balance
776 quantified by optical remote sensing on 30 glaciers in the French Alps for the period 1983–2014, *J.*
777 *Glaciol.*, 62(236), 1153–1166, doi:10.1017/jog.2016.113, 2016.
- 778 Sirguey, P.: Simple correction of multiple reflection effects in rugged terrain, *Int. J. Remote Sens.*,
779 30(4), 1075–1081, doi:10.1080/01431160802348101, 2009.
- 780 Sirguey, P., Mathieu, R., Arnaud, Y., Khan, M. M. and Chanussot, J.: Improving MODIS Spatial
781 Resolution for Snow Mapping Using Wavelet Fusion and ARSIS Concept, *IEEE Geosci. Remote Sens.*
782 *Lett.*, 5(1), 78–82, doi:10.1109/LGRS.2007.908884, 2008.
- 783 Sirguey, P., Mathieu, R. and Arnaud, Y.: Subpixel monitoring of the seasonal snow cover with MODIS
784 at 250 m spatial resolution in the Southern Alps of New Zealand: Methodology and accuracy
785 assessment, *Remote Sens. Environ.*, 113(1), 160–181, doi:10.1016/j.rse.2008.09.008, 2009.



- 786 Sirguey, P., Still, H., Cullen, N. J., Dumont, M., Arnaud, Y. and Conway, J. P.: Reconstructing the
787 mass balance of Brewster Glacier, New Zealand, using MODIS-derived glacier-wide albedo, *The*
788 *Cryosphere*, 10(5), 2465–2484, doi:10.5194/tc-10-2465-2016, 2016.
- 789 Six, D., Wagnon, P., Sicart, J. E. and Vincent, C.: Meteorological controls on snow and ice ablation for
790 two contrasting months on Glacier de Saint-Sorlin, France, *Ann. Glaciol.*, 50(50), 66–72,
791 doi:10.3189/172756409787769537, 2009.
- 792 Stocker, T., Qin, D., Plattner, G., Tignor, M., Allen, S., Boschung, J., Nauels, A., Xia, Y., Bex, B. and
793 Midgley, B.: IPCC, 2013: climate change 2013: the physical science basis. Contribution of working
794 group I to the fifth assessment report of the intergovernmental panel on climate change, 2013.
- 795 Van As, D.: Warming, glacier melt and surface energy budget from weather station observations in the
796 Melville Bay region of northwest Greenland, *J. Glaciol.*, 57(202), 208–220,
797 doi:10.3189/002214311796405898, 2011.
- 798 Vincent, C.: Influence of climate change over the 20th Century on four French glacier mass balances, *J.*
799 *Geophys. Res. Atmospheres*, 107(D19), 4375, doi:10.1029/2001JD000832, 2002.
- 800 Vincent, C., Vallon, M., Reynaud, L. and Le Meur, E.: Dynamic behaviour analysis of glacier de Saint
801 Sorlin, France, from 40 years of observations, 1957–97, *J. Glaciol.*, 46(154), 499–506,
802 doi:10.3189/172756500781833052, 2000.
- 803 Wang, W., Zender, C. S., van As, D., Smeets, P. C. J. P. and van den Broeke, M. R.: A Retrospective,
804 Iterative, Geometry-Based (RIGB) tilt-correction method for radiation observed by automatic weather
805 stations on snow-covered surfaces: application to Greenland, *The Cryosphere*, 10(2), 727–741,
806 doi:10.5194/tc-10-727-2016, 2016.
- 807 Wolfe, R. E., Roy, D. P. and Vermote, E.: MODIS land data storage, gridding, and compositing
808 methodology: Level 2 grid, *IEEE Trans. Geosci. Remote Sens.*, 36(4), 1324–1338,
809 doi:10.1109/36.701082, 1998.
- 810 Zemp, M., Frey, H., Gärtner-Roer, I., Nussbaumer, S. U., Hoelzle, M., Paul, F., Haeberli, W.,
811 Denzinger, F., Ahlstrøm, A. P., Anderson, B., Bajracharya, S., Baroni, C., Braun, L. N., Cáceres, B. E.,
812 Casassa, G., Cobos, G., Dávila, L. R., Delgado Granados, H., Demuth, M. N., Espizua, L., Fischer, A.,
813 Fujita, K., Gadek, B., Ghazanfar, A., Hagen, J. O., Holmlund, P., Karimi, N., Li, Z., Pelto, M., Pitte, P.,
814 Popovnin, V. V., Portocarrero, C. A., Prinz, R., Sangewar, C. V., Severskiy, I., Sigurðsson, O., Soruco,
815 A., Usubaliev, R. and Vincent, C.: Historically unprecedented global glacier decline in the early 21st
816 century, *J. Glaciol.*, 61(228), 745–762, doi:10.3189/2015JoG15J017, 2015.
- 817